Duane D. Blatter, MD • Dennis L. Parker, PhD • Ronald O. Robison, MD

Cerebral MR Angiography with Multiple Overlapping Thin Slab Acquisition

Part I. Quantitative Analysis of Vessel Visibility[1]

Multiple overlapping thin slab acquisition (MOTSA) is a novel time-of-flight magnetic resonance (MR) angiography technique that combines many of the advantages of multiple-section two-dimensional and direct three-dimensional volume methods. To rigorously evaluate the vascular detail that can be obtained with MOTSA MR angiography, the authors have quantified the frequency of visibility of intracranial arterial segments and have correlated their visibility with vessel size as measured at cut-film angiography and with the position and orientation of the arterial segment. Intracranial arterial segments at least 0.9 mm in diameter (the voxel dimension used in the current application) are consistently visualized with the MOTSA technique. The fraction of small vessels visualized is improved when voxel dimensions are reduced. Visibility is noticeably better in the primary images compared with the maximum-intensity-projection (MIP) images. Top-of-slab saturation and resulting decreased vessel intensity occurred infrequently and did not result in marked image degradation in the axial images.

Index terms: Cerebral blood vessels, MR studies, 17.1214 • Magnetic resonance (MR), image processing • Magnetic resonance (MR), technology • Magnetic resonance (MR), vascular studies, 17.1214

Radiology 1991; 179:805–811

[1] From the Departments of Radiology, LDS Hospital (D.D.B.) and Medical Informatics, LDS Hospital and University of Utah (D.L.P., R.O.R.), Eighth Ave and C St, Salt Lake City, UT 84143. From the 1990 RSNA scientific assembly. Received October 1, 1990; revision requested November 26; revision received January 21, 1991; accepted February 14. Supported by a grant from the Deseret Foundation of the LDS Hospital. **Address reprint requests to** D.D.B.

THE sensitivity of magnetic resonance (MR) imaging to flow and its lack of known harmful side effects has led to significant interest in MR angiography techniques that might replace at least some standard intra-arterial angiographic procedures. In recent years there has been significant progress in the development of MR angiography techniques due to improvements in MR imager hardware and pulse sequence design and the introduction of nonlinear display algorithms such as maximum intensity projection (MIP) (1).

Because of the great flexibility allowed with MR imaging, there is great variability in the angiography techniques that have been developed. Techniques are available to acquire image data as a densitometric projection through the object; these techniques generate images that are very similar to conventional angiograms (2–11). Other techniques acquire the image data directly as a three-dimensional array of small image elements (voxels) (12–16). For both projection techniques and techniques that acquire image data as three-dimensional arrays of voxels, the image data can be acquired sequentially from thin sections through the region of interest or from a complete three-dimensional volume. The signal obtained can be due to a velocity-dependent phase shift (phase contrast) (6–12) or a relative increase in signal amplitude due to the inflow of fresh, nonsaturated magnetization into the imaging region (amplitude contrast or "time of flight") (2–5,13–16).

Many distinct advantages and disadvantages to the various imaging techniques exist. For example, projection techniques are relatively fast in generating a single view of the artery of interest. However, the imaging sequence must be repeated for additional views and there is significant signal loss due to phase dispersion along the long projection dimension. Techniques used to acquire image data in three-dimensional arrays, such as multiplanar two-dimensional or direct three-dimensional acquisition, have demonstrated good vessel detail when vessels are reprojected by using the MIP display algorithm (17,18). The multiplanar two-dimensional techniques work well for vessels that are perpendicular to the section, but the moderately large thickness of the section (approximately 2.5 mm) causes a loss in signal due to phase dispersion when the vessel is not perpendicular to the section (see, for example, Haacke et al [19]). Direct three-dimensional volume acquisition, time-of-flight techniques have the advantage of very low noise (due to the inherent signal averaging of three-dimensional techniques) and also result in low vessel signal due to the longer time the blood remains in the thick section being imaged (20).

In spite of the various disadvantages, amplitude-contrast (time-of-flight) techniques seem to be less sensitive to machine-dependent distortions of the gradient waveforms and can therefore be conveniently implemented on most MR imagers. To use this advantage of amplitude-contrast techniques and to attempt to combine the advantages of two-dimensional multiplanar and direct three-dimensional acquisition techniques, we have developed a multiple-overlapping-thin-slab-acquisition (MOTSA) technique at the LDS Hospital and University of Utah (21,22).

MOTSA maintains the improved signal-to-noise ratio, simultaneous thin-section imaging, and short echo time (TE) that are important advantages of three-dimensional acquisi-

Abbreviations: MIP = maximum intensity projection, MOTSA = multiple overlapping thin-slab acquisition, TE = echo time, TR = repetition time.

tion, and also preserves the high signal intensity from fresh, unsaturated spins, the characteristic advantage of two-dimensional multiplanar methods. The thin section thickness (typically, 0.94 mm) and short TE (5.5 msec) further reduce the sensitivity of the technique to phase dispersion. The MOTSA technique, which consists of acquiring image data in multiple overlapping regions (thin slabs), is generally applicable in that one can acquire an arbitrary (power of two) number of sections per slab and an arbitrary number of slabs; in addition, the slabs can be interleaved during data acquisition to increase the effective repetition time (TR). Image quality with use of the short TE and moderately thin slab dimensions has been consistently good.

Although several MR angiography techniques have undergone preliminary clinical evaluation, and in some institutions are being used routinely in clinical applications, to our knowledge no reports of attempts to quantitatively evaluate vessel visibility have been published. To begin such an evaluation of the quality of vascular detail that can be obtained from the MOTSA MR angiography technique, we performed a study of the visibility of major intracranial vessels in which we quantified the frequency of visibility of various intracranial arterial segments and correlated their visibility with vessel size as measured at standard cut-film, contrast material–enhanced angiography.

MATERIALS AND METHODS

Intracranial MR angiograms of 23 individuals (12 healthy volunteers and 11 patients) were included in a nonselective, prospective fashion. The average age of each subject was 43.1 years (range, 27–68 years). The 11 patients underwent standard contrast-enhanced angiography. All subjects signed an informed consent form, which had been approved by the hospital's institutional review board.

All MR angiographic studies were performed with use of an unmodified 1.5-T MR imager (Signa; GE Medical Systems, Milwaukee), with use of standard patient position, a quadrature head coil, and conventional sagittal T1-weighted spin-echo imaging for localization. MR angiography was performed by using the MOTSA technique. The MOTSA pulse sequence, theory, and performance in flow phantoms have been described in detail elsewhere (21,22). The pulse sequence is diagrammed in Figure 1.

MOTSA consists of the acquisition of multiple thin regions (slabs) that are each phase encoded in the section-selective direction in such a manner that three-dimensional, Fourier-transform reconstruction results in a small set of very thin sections from each slab. Each slab is a gradient-recalled three-dimensional acquisition that derives enhanced blood contrast from the time-of-flight (amplitude) contrast effect of fresh, unsaturated blood magnetization flowing into the thin slab being imaged.

Conceptually, the MOTSA technique is generally applicable in that one can acquire an arbitrary number of sections per slab (this must be a power of two) and an arbitrary number of slabs with an arbitrary amount of overlapping between adjacent slabs; in addition, the slab acquisition can be interleaved to increase the effective TR. In our experience an interleaved acquisition (two slabs acquired simultaneously, separated by four slabs) can be obtained without any apparent loss in signal-to-noise ratio or vessel visibility. The geometry of the slabs and sections is shown in Figure 2.

The implementation that has been most successful and that was used in these studies consists of use of a 12-mm-thick slab of excitation, which is centered in a 15-mm-thick imaging volume. Sixteen phase-encoding steps in the z direction (when imaging is in the axial plane) yields a section thickness of 0.94 mm (16 sections, each 15 mm thick). The slabs are then acquired sequentially with 50% overlap (slab spacing of 7.5 mm) so that the central eight sections of each overlapping slab form a continuous three-dimensional data set. Only the central eight sections of each slab were reconstructed initially in this study. In the later studies (Fig 3), the central 12 sections of each slab were reconstructed, and the overlapping sections were combined by using the brightest pixel, on a pixel-by-pixel basis.

Overlapping of the slabs was necessary for two reasons. First, as with any volume-acquisition technique, wraparound occurred in each phase-encoding direction. To avoid phase wrap in the z direction only, the central region of the imaged volume was excited by the selective resonance-frequency pulse, and the first and last sections were discarded. Second, the profile of the resonance-frequency excitation pulse was not a pure square wave (Fig 2), and overlapping allowed the use of a wider excitation pulse, with the central eight sections occupying the flatter central portion of the profile. Without use of these techniques, reprojected MIP images would have suffered unacceptably from slab interface or "venetian blind" artifact.

To shorten the TE as much as possible, we employed both an asymmetric resonance-frequency excitation pulse and an asymmetric echo readout (ie, fractional echoes), as recently described by Schmalbrock et al (23). By truncating the resonance-frequency excitation sinc pulse after the first null point following the central lobe, and by placing the center of the echo asymmetrically within the readout window (Fig 1), the TE could be reduced by a total of 5.5 msec. With first-order

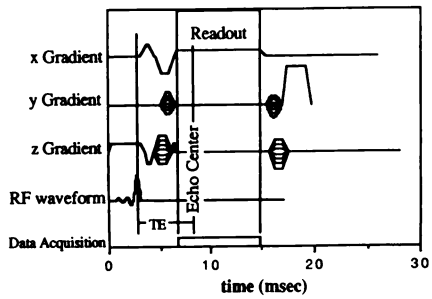

Figure 1. Diagram of the MOTSA pulse sequence. Note the asymmetric echo window and truncated sinc pulse, which allows use of a shortened TE of 5.5 msec. Zero- and first-order flow compensation is shown in the z gradient.

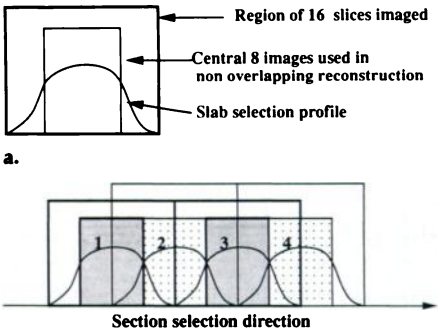

Figure 2. Diagram of the section excitation profile **(a)** and the geometry of overlapping slabs and sections **(b)** in the MOTSA technique.

flow compensation on the section-selective and readout gradients, the effective TE, from the central lobe of the truncated sinc pulse to the center of the echo, was 5.5 msec. A flip angle of 30° was employed.

In 18 cases, the study consisted of nine slabs acquired sequentially (noninterleaved) with use of a TR of 50 msec and 128 phase-encoding steps (256 × 128 imaging matrix). This allowed imaging from the foramen magnum to well above the circle of Willis, with an acquisition time of 15 minutes. In five cases (three healthy volunteers and two patients), seven slabs were acquired in an interleaved fashion, with use of a TR of 70 msec and 256 phase-encoding steps (256 × 256 imaging matrix); the time required for imaging was 19 minutes. A 24-cm field of view was employed in all cases.

The 11 patients underwent standard contrast-enhanced angiography with use of a cut-film, magnification technique. The focal-object and focal-film distances of each projection were standardized and measured; the magnification factors were calculated and were used for correcting each measurement of lumen diameter. For each vessel segment of interest, the presence or absence of the vessel was noted and lumen diameter was measured on both direct contrast-enhanced and sub-

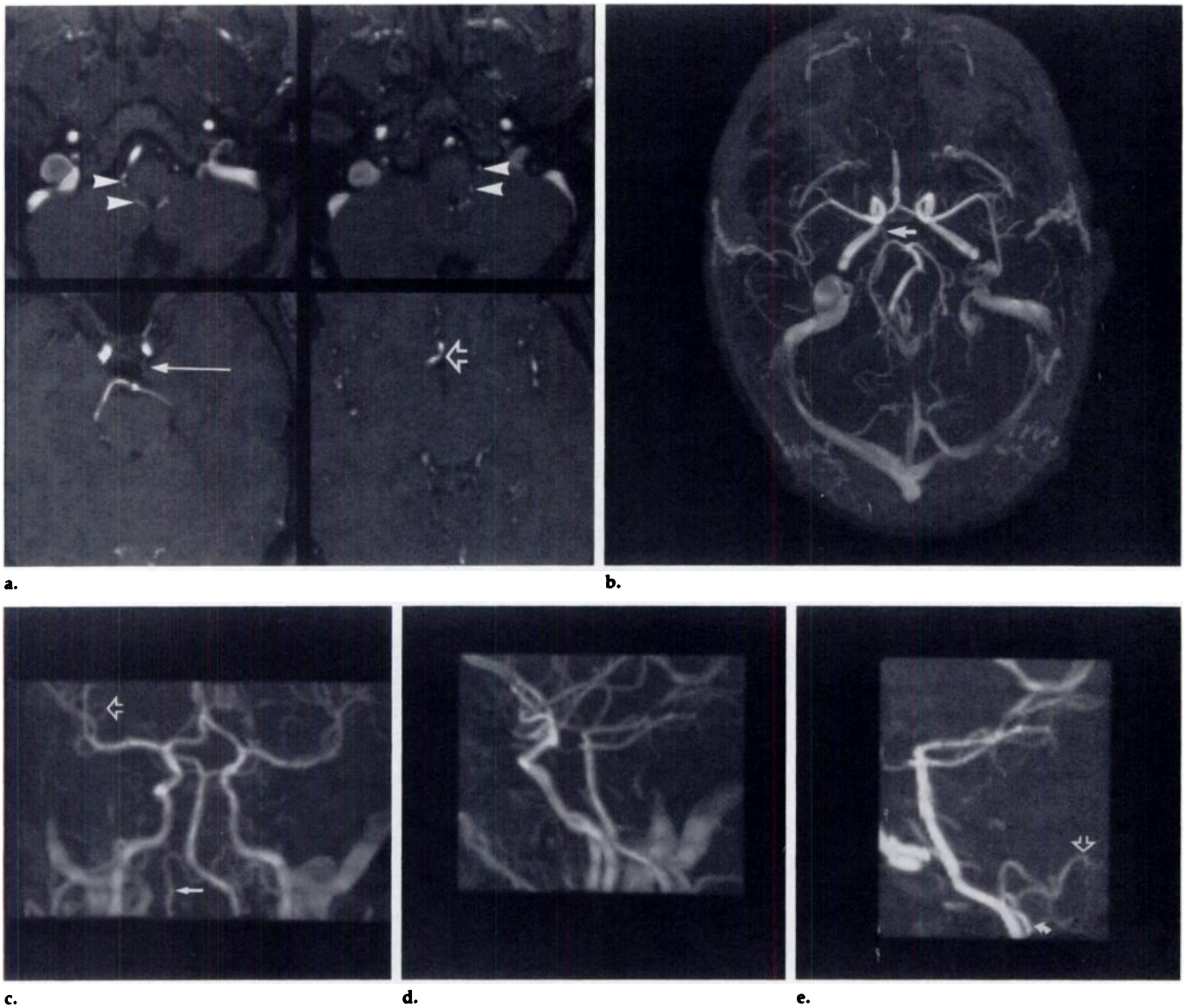

Figure 3. Typical MOTSA MR angiograms of a healthy volunteer include a volume from the foramen magnum to well above the circle of Willis. **(a)** Examples of limited regions from axial images from the level of the posterior inferior cerebellar artery (arrowheads), a small left posterior communicating artery (solid arrow), and the anterior cerebral arteries at the level of the anterior communicating artery (open arrow). **(b)** Base projection MIP image (collapse). A large right posterior communicating artery is seen (arrow), while the small left posterior communicating artery demonstrated in the axial image in **a** is not visible. Frontal **(c)** and lateral **(d)** MIP images demonstrate a congenitally small right vertebral artery terminating as a posterior inferior cerebellar artery (solid arrow in **c**). Second-order middle cerebral artery branches within the sylvian fissure (open arrow in **c**) are clearly demonstrated, without degradation of visibility due to saturation. **(e)** Lateral MIP image of a more restricted region of the posterior fossa. The venous sinuses have been excluded, and the posterior inferior cerebellar arteries can be seen continuously from their origin (curved arrow) through the cranial loop (open arrow) and at their division into hemispheric branches.

tracted MR angiograms.

Analysis of MR angiograms was performed by using both the original axial images and the angiographic projections that were generated by means of a standard MIP ray-tracing algorithm (Irma, GE Medical Systems). For each data set, a total of 30 MIP images obtained at 6° increments through 180° rotation about an axis perpendicular to the axial plane (coronal → sagittal → coronal) were generated.

The MIP images were generated by using a tightly restricted, rectangular subregion that included the area from sylvian fissure to sylvian fissure and from anterior to the pericallosal artery to just posterior to the quadrigeminal cistern. No threshold was applied in generating the MIP images. All suppression of background soft tissue was the result of saturation.

Images were evaluated for the visibility of each of the major intracranial segments by a single neuroradiologist (D.D.B.) (Table). The direct axial and MIP images were evaluated separately. Each vessel segment was determined to be either visible or not visible. The criteria for visibility of each vessel were (*a*) linear structure present in the expected anatomic location, (*b*) visibility at the origin from the parent vessel and continuously for at least a 4-mm segment, and (*c*) visibility on MIP images at multiple reprojection angles. The signal loss secondary to saturation, when present, was noted for the internal carotid and anterior, middle, and posterior cerebral arteries. The percentage of visibility for each vessel segment was correlated with lumen diameter (determined angiographically) and vessel location and orientation.

RESULTS

Sample images that illustrate the quality of MR angiograms of the 23 subjects are shown in Figure 3. The vessel detail in these images is excel-

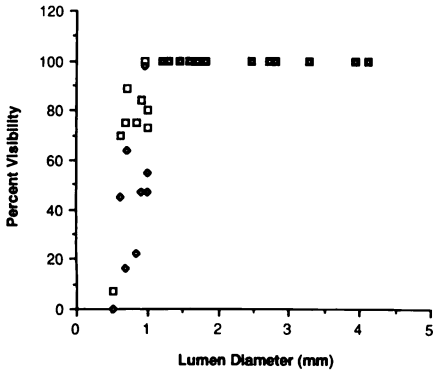

Figure 4. Plot of percentage of visibility of each intracranial arterial segment as a function of lumen diameter as measured from standard cut-film angiograms. Percentage of visibility in direct axial images is shown with open boxes; the percentage of visibility in MIP images is shown with open diamonds.

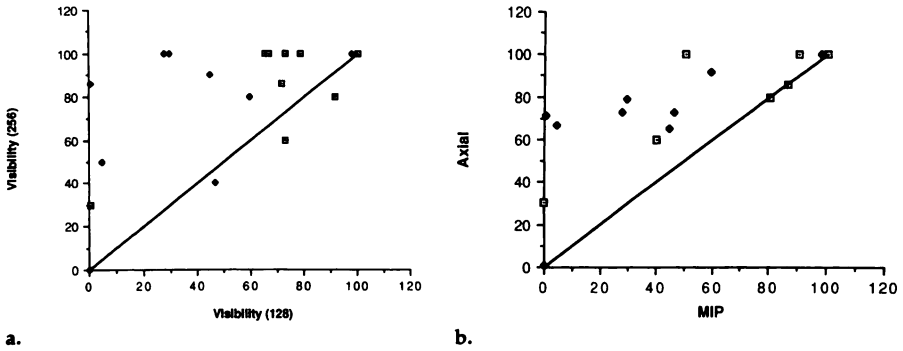

Figure 5. Vessel visibility as a function of **(a)** the y phase-encoding resolution (128 vs 256 encodings) and **(b)** the display method. Percentage of visibility in direct axial images is shown with boxes; the percentage of visibility in MIP images is shown with solid diamonds.

lent. In general, comparable image quality was obtained for all subjects.

Results of the visibility analysis are given in the Table. These data include observations of visibility from both axial and MIP images. The Table consists of the combined observations of all 23 images and a separate analysis of observations of only those images that were obtained with use of 256 y phase encodings. In seven of nine arterial segments with a lumen diameter of 1.0 mm or less the percentage of visibility was much higher with use of 256 phase encodings compared with use of 128 encodings. In two of these nine segments, the observed visibility was slightly lower with 256 encodings, presumably reflecting statistical variation (in each case the difference in percentage of visibility between the 256-encodings and 128-encodings groups was not more than one additional arterial segment from a total of 10 segments). These observations are plotted in Figures 4 and 5.

In Figure 4 the percentage of visibility for each vessel segment was plotted as a function of the corresponding mean lumen diameter as measured from the standard angiograms. In Figure 5 the visibility of the various vessel segments as a function of the number of y phase encodings and of the display algorithm was compared. From Figure 5a it is evident that the small vessel segments are consistently more visible in the axial images than in the MIP images. From Figure 5b it is evident that vessel visibility is also improved by using a higher resolution imaging matrix (256 rather than 128 y phase encodings).

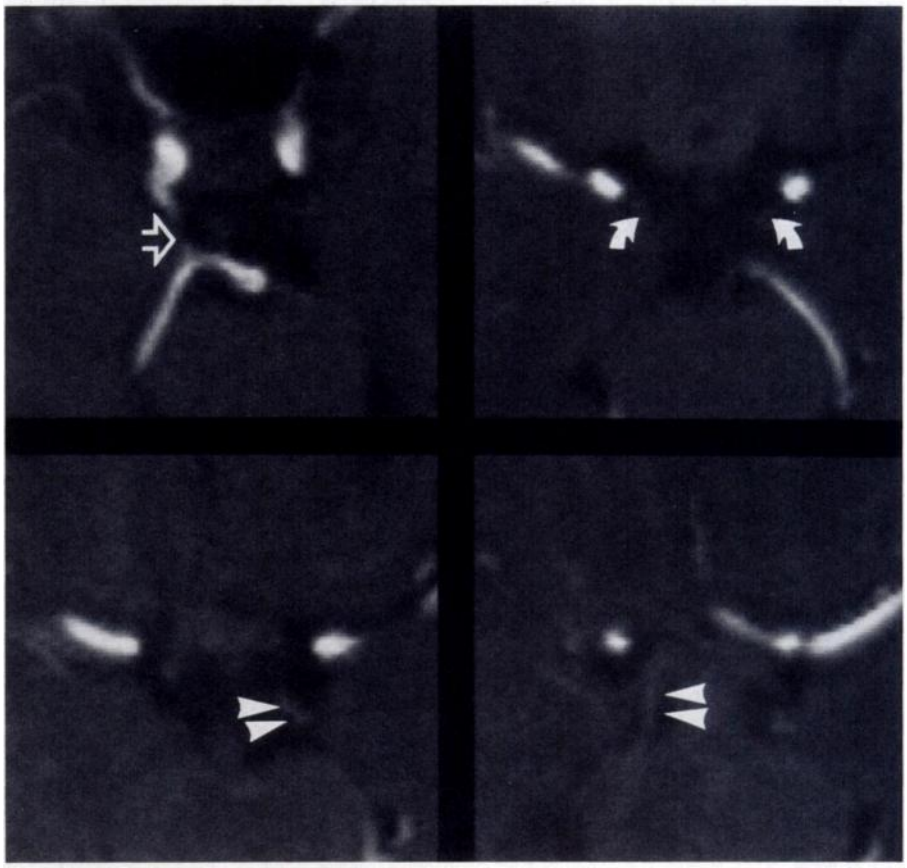

Figure 6. The normal anterior choroidal artery demonstrated on direct axial images obtained with 256 y phase-encoding resolution. Right posterior communicating artery (open arrow) and anterior choroidal artery (curved arrow) are seen bilaterally. On contiguous images beginning at its origin 4 mm above the posterior communicating artery, the anterior choroidal artery is seen in its cisternal course medial to the uncus of the temporal lobe (arrowheads).

The internal carotid artery was visible in 100% of cases. A mild decrease in signal intensity in the cavernous and supraclinoid carotid artery was seen in four of 46 arteries (9%), a finding that was always associated with a redundant, looping artery. The effect was also more prominent in patients with generalized arteriomegaly, with resultant lower blood velocity. Thirty-nine of 44 ophthalmic arteries (89%) were visible on axial images for a variable length, ranging from 4 to 11 mm. The anterior choroidal artery was not visible in any images that were acquired with use of 128 y phase-encoding resolution in the phase-encoding direction. Five of 10 anterior choroidal arteries that were imaged with use of a 256 ×

Vessel Visibility and Lumen Diameter at MR Angiography

Artery	Vessel Visibility: Direct Axial Images* All	Direct Axial Images* 256 Encodings	MIP Images* All	MIP Images* 256 Encodings	No. of Images All	No. of Images 256 Encodings	Lumen Diameter Mean (mm)	Lumen Diameter SD
Internal carotid								
Petrous	100	100	100	100	44	10	4.08	0.31
Cavernous	100	100	100	100	46	10	3.90	0.45
Supraclinoid	100	100	100	100	46	10	3.25	0.41
Bifurcation	100	100	100	100	46	10		
Ophthalmic	89	80	64	80	44	10	0.71	0.22
Anterior choroidal	11	50	0	0	46	10	0.52	0.06
Posterior communicating	73	100	55	90	44	10	1.01	0.24
Anterior cerebral								
Precommunical	100	100	100	100	45	10	1.67	0.38
Communicating	100	100	100	100	23	5	...	...
Pericallosal	100	100	100	100	46	10	1.52	0.31
Middle cerebral								
Horizontal	100	100	100	100	46	10	2.46	0.26
Trifurcation	100	100	100	100	46	10	NA	NA
Sylvian	100	100	100	100	46	10	1.42	0.28
Vertebral	100	100	100	100	34	10	2.78	0.86
Posterior inferior cerebellar								
Anterior medullary	80	100	47	100	30	8	1.01	0.22
Lateral medullary	84	100	47	100	32	8	0.91	0.23
Posterior medullary	75	86	22	86	32	8	0.84	0.14
Supratonsilar	75	100	16	50	32	8	0.70	0.11
Basilar	100	100	100	100	23	5	2.76	0.53
Anterior inferior cerebellar	70	60	45	40	44	10	0.62	0.15
Superior cerebellar	100	100	98	100	46	10	0.96	0.22
Posterior cerebral								
Interpeduncular	100	100	100	100	46	10	1.60	0.23
Ambient	100	100	100	100	46	10	1.51	0.23
Quadrigeminal	100	100	100	100	46	10	1.26	0.24

* Numbers indicate percentage of visibility.

256 matrix were visible on axial images (Fig 6). None of these arteries were visible on MIP images. The bifurcation of the internal carotid artery was well displayed in all cases.

The anterior cerebral artery complex was consistently well imaged at MR angiography. Mild saturation of the horizontal (precommunical) segment was seen in six of 46 arteries (13%). The normal anterior communicating artery was well displayed in all 23 cases, either as a discrete artery or as a short communication between the two anterior cerebral arteries, and was equally well shown in both axial and MIP images. The MIP images were particularly useful in unfolding the frequent overlapping of the pericallosal arteries. Two normal variants were confirmed at MR angiography: an absent precommunical anterior cerebral artery and a single pericallosal artery (azygous artery). The absent precommunical anterior cerebral artery was demonstrated by filling of both pericallosal arteries from the contralateral side through the anterior communicator.

The horizontal segment of the middle cerebral artery was always visible from the bifurcation of the internal carotid artery to the sylvian fissure. On MIP images, significant saturation secondary to prolonged in-plane flow was apparent in the distal horizontal segment in eight of 46 arteries (17%). However, even in the most severely affected vessels, the trifurcation was well defined on axial images. First- and second-order branches of the middle carotid artery within the sylvian fissure were seen in all cases. No normal perforating arteries arising from either the middle carotid artery or the anterior cerebral artery were visible. The case of a clearly visible perforator from the middle carotid artery in a patient with a deep left temporal lobe astrocytoma is shown in Figure 7. This vessel measured 0.55 mm in diameter on the contrast-enhanced angiogram; this diameter is slightly larger than normal because the vessel was supplying the tumor.

The posterior communicating artery was visible at MR angiography 73% of the time; the direct axial images were clearly superior to the MIP images (73% vs 55%, respectively). Visibility increased to 90% in the group of images made with use of the 256 × 256 resolution. In the group of patients who underwent intraarterial angiography, the average lumen diameter of the posterior communicating artery was 1.01 mm, with a larger standard deviation than that of the diameters of other arteries. The posterior communicating artery was either very small (0.6 mm or less) or absent in four of 16 (25%), which is consistent with prior reports (24). The posterior cerebral artery, including the interpeduncular ambient and quadrigeminal segments, was always visible, as were second-order branches in the interhemispheric fissure.

The vertebral artery at the axis loop consistently demonstrated decreased intensity secondary to saturation. All vertebral and basilar arteries were visible. The origins of the posterior inferior cerebellar artery were visible 80% of the time on axial images (Fig 3e). Dominant anterior inferior cerebellar arteries accounted for most of the nonvisible posterior inferior cerebellar artery systems. The MIP images were severely limited in this region because of multiple overlying venous sinuses, which were present unless images were obtained of only a very restricted region. The superior cerebellar artery was always visible, making it the smallest artery (0.96 mm in diameter) with 100% visibility. Two cases of persistent trigeminal artery communication (embryologic precavernous carotid to basilar) were noted, one of which was confirmed at intraarterial angiography.

The principal artifact associated with the imaging technique appeared to be a variation in intensity at the slab interfaces, a finding that was seen in all of the figures shown herein. This variation in intensity was due to two phenomena: (*a*) nonrectangular excitation profile (Fig 2) and (*b*) decrease in the signal intensity of blood as a function of saturation due to the time spent (number of excitation pulses experienced) within the boundaries of the slab. The saturation component of this effect was most severe in patients with tortuous and enlarged vessels. There was, however, no case of significant loss of anatomic detail on axial images.

DISCUSSION

Many factors can potentially affect vessel visibility at MR angiography, including anatomic factors such as vessel diameter, orientation, and direction and velocity of flow. Surrounding tissues (particularly fat), when incompletely saturated, can significantly decrease vessel visibility by reducing the contrast-to-noise ratio. Vessel contrast is also affected by imaging parameters such as TR, TE, flip angle, slab thickness and orientation, and effective voxel size.

Several observations are evident from the results presented herein. First, it is evident from the observations demonstrated in the Table and in Figure 4 that the single most important factor in determining the visibility of a vessel is the diameter of the lumen. Factors such as vessel orientation and position within the imaged volume had remarkably little effect. All vessels with a lumen diameter larger than the voxel dimensions used at MR angiography were consistently visualized. The visibility of vessels that were near the resolution limit decreased rapidly to zero as the vessel diameter decreased. The potential for improved visibility with increased resolution was indicated from the comparative visibility of vessels when 256 y phase encodings were used compared with 128 y phase encodings (Fig 5). In the latter case, the effective pixel dimension in the y direction was double the 0.94-mm dimension in the higher resolution images. Similar improvement in small vessel visibility with use of decreasing voxel size has also been observed in previous reports (14,25).

As shown in the Table and in Figure 4, we also observed that small vessel visibility was significantly better in the original axial images than in the MIP images. This effect was due in large part to the reduced intensity of the blood signal in the smaller vessels. If the blood signal intensity drops below the level of the signal intensity of surrounding structures, the vessel will not appear in an MIP image. Occasionally the signal intensity of a vessel was near that of the surrounding background structures. In that case, random noise in the surrounding structures occurred over a much longer projection dimension than occurred over the vessel itself. Therefore, the maximum pixel intensity along any given path through the vessel probably came from a noise peak that was external to the vessel. Vessel visibility could therefore be improved by generating the MIP images on adjacent subregions. The visibility reported herein was for MIP images that were focused on the smallest possible subregion that included the arterial segments to be studied. Generating images of subregions around each individual segment increases visibility, but this method would not be practicable in routine clinical application. The unavoidable loss of information about small vessels that results when a three-dimensional data set is projected into a two-dimensional MIP image has been similarly observed by Anderson et al (26) and Ross et al (27).

Single-volume, three-dimensional, time-of-flight MR angiography techniques are known to be affected by significant saturation of vessel signal when the volumes required for routine clinical studies are used (20). The degree of saturation is dependent on the flip angle, TR, blood velocity, volume thickness, and geometry of the vessel (which reflects time spent in the volume). We have reported the explicit mathematical solution to vessel signal as a function of each of these variables. We have shown that MOTSA is theoretically the most efficient method (in terms of signal-to-noise ratio) by which to perform three-dimensional MR angiography (22). Unlike direct, three-dimensional, time-of-flight MR angiography, in which vessels at the top of any large volume are degraded by saturation, with use of MOTSA imaging, vessels at the top of the imaged volume are seen equally well as vessels at the bottom. Saturation of vessel signal, which is due to prolonged time within the imaging slab, occurred infrequently and was seen only in those vessel segments that were present for a prolonged time within a given slab,

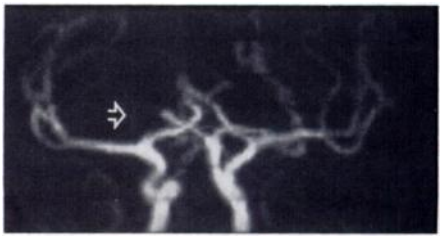

a.

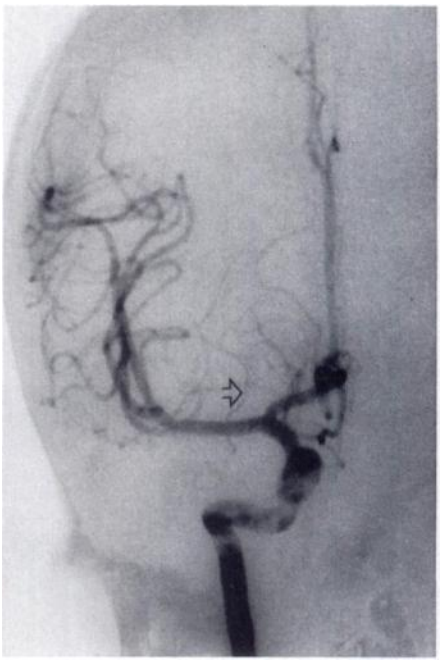

b.

Figure 7. Frontal views from an MOTSA MR angiogram **(a)** and a conventional contrast-enhanced angiogram **(b)** in a patient with a deep right temporal lobe astrocytoma. Lateral displacement of sylvian branches of the middle cerebral artery is apparent in both studies. An enlarged perforator (0.55 mm) is seen in both studies (open arrow in **a** and **b**). The series of direct axial images (not shown) clearly demonstrated that this perforator originated from the horizontal middle cerebral artery and terminated within the deep temporal glioma.

such as the horizontal middle cerebral artery and the precommunical anterior cerebral artery. This saturation effect was most evident on MIP images, and vessel detail was not seriously degraded on the direct axial images.

The principal disadvantage of MOTSA appears to be the variation in signal intensity at slab boundaries, an appearance which we refer to as the "venetian blind" artifact. The effect is exaggerated on the MIP images; when the direct axial images are analyzed, little real distortion is apparent. The effect can be minimized on MIP images by using any projection that is angled with respect to the plane of the original data ac-

quisition (axial for the data presented here). This technique was not used for display of any of the images shown herein.

The venetian blind artifact has two principal causes: a nonsquare section profile and saturation of the top of the slab. The venetian blind artifact is a potentially serious obstacle to use of the MOTSA technique. Any successful application of MOTSA MR angiography must be accomplished with an understanding of the appearance and causes of this artifact and must include strategies for minimizing its effect. A recent article by Marchal et al (28) reported improved vessel visibility in three-dimensional MR angiograms when the volumes were kept thin and when overlapping volumes were acquired with sequential table incrementation, an approach similar to that described herein. There was, however, no discussion of the slab interface or venetian blind artifact or its effect on vessel visibility and diagnostic quality. Only MIP collapse images were shown (submentovertex view when axial partitions were acquired), in which the venetian blind artifact was not apparent.

Reduction in this artifact can be achieved through improvements in acquisition and examination after processing. During acquisition, excitation pulses with more nearly rectangular section profiles can be applied, as well as minor widening of the profile width. In addition, the physical overlapping of slabs in the MOTSA technique described herein allows much of the venetian blind artifact to be removed by careful computerized postprocessing. Since the edge sections of each slab are from the same physical location as are the center sections of adjacent slabs, the weak image detail from the edge sections can be replaced by the strong image detail of the corresponding central sections. We have developed and are evaluating a program that combines data from the overlapping sections by selecting, pixel by pixel, the brightest of the corresponding points. Preliminary results with use of these strategies are promising.

We conclude that MOTSA is a promising new time-of-flight MR angiography technique that combines many of the advantages of previous two-dimensional and three-dimensional techniques. Intracranial arterial segments larger than the pixel dimensions (0.9 mm in the current application) are consistently visualized with use of the MOTSA technique; the fraction of small vessels visualized is improved when the size of effective voxel dimensions is reduced. Visibility is significantly better when the original axial images are used rather than maximum-intensity reprojections.

The MOTSA technique can have a number of applications. We have presented results from only one specific implementation of the technique. It is certainly possible that other variations in this technique might improve the results we have obtained. It is also likely that other variations will be useful in obtaining images of arteries in other anatomic regions, such as carotid arteries in the neck and peripheral arteries. Further work is needed to establish this usefulness. ■

Acknowledgments: The authors thank Julie Cha, Gerry Gelaco, and Kathy Taylor for technical assistance and Connie Cates for help in manuscript preparation.

References

1. Rossnick S, Laub G, Braeckle R, et al. Three dimensional display of blood vessels in MRI. In: Proceedings of the IEEE computers cardiology conference. New York: New York Institute of Electrical and Electronic Engineers, 1986; 193–196.
2. Nishimura DG, Macovski A, Pauly JM, Conolly SM. MR angiography by selective inversion recovery. Magn Reson Med 1987; 4:193–202.
3. Nishimura DG, Macovski A, Pauly JM. Consideration of magnetic resonance angiography by selective inversion recovery. Magn Reson Med 1988; 7:472–484.
4. Nishimura DG, Macovski A, Jackson JI, Hu RS, Stevick CA, Axel J. Magnetic resonance angiography by selective recovery using a compact gradient echo sequence. Magn Reson Med 1988; 8:96–103.
5. Frahm J, Merboldt KD, Hanicke W, Gyngell ML, Bruhn H. Rapid line scan NMR angiography. Magn Reson Med 1988; 7:79–87.
6. Dumoulin CL, Souza SP, Feng H. Multiecho magnetic resonance angiography. Magn Reson Med 1987; 5:47–57.
7. Dumoulin CL, Souza SP, Walker MF, Yoshitome E. Time-resolved magnetic resonance angiography. Magn Reson Med 1988; 6:275–286.
8. Dumoulin CL, Souza SP, Hart HR. Rapid scan magnetic resonance angiography. Magn Reson Med 1987; 5:238–245.
9. Chenevert TL, Fechner KP, Gelblum DY. Improvements in MR angiography using phase-corrected data sets. Magn Reson Med 1989; 10:38–49.
10. Tasciyan TA, Lee JN, Riederer SJ, et al. Fast limited flip angle MR subtraction angiography. Magn Reson Med 1988; 8:261–274.
11. Lee JN, Riederer SJ, Pelc NJ. Flow-compensated limited flip angle MR angiography. Magn Reson Med 1989; 12:1–13.
12. Wagle WA, Dumoulin CL, Souza SP, Kleine HE. 3DFT MR angiography of carotid and basilar arteries. AJNR 1989; 10:911–919.
13. Dumoulin CL, Cline HE, Souza SP, Wagle WA, Walker MF. Three-dimensional time-of-flight magnetic resonance angiography using spin saturation. Magn Reson Med 1989; 11:35–46.
14. Ruggieri PM, Laug GA, Masaryk TJ, Modic MT. Intracranial circulation: pulse-sequence considerations in three-dimensional (volume) MR angiography. Radiology 1989; 171:785–791.
15. Gullberg GT, Wehrli FW, Shimakawa A, Simons MA. MR vascular imaging with a fast gradient refocusing pulse sequence and reformatted images from transaxial sections. Radiology 1987; 165:241–246.
16. Wehrli FW, Shimakawa A, Gullberg GT, MacFall JR. Time-of-flight MR flow imaging: selective saturation recovery with gradient refocusing. Radiology 1986; 160:781–785.
17. Keller PJ, Drayer BP, Fram EK, Dumoulin CL, Souza SP. 2D magnetic resonance arteriography of the neck (abstract). Magn Reson Imaging 1989; 7(suppl 1):186.
18. Keller PJ, Drayer BP, Fram EK, Williams KD, Dumoulin CL, Souza SP. MR angiography with two-dimensional acquisition and three-dimensional display: work in progress. Radiology 1989; 173:527–532.
19. Haacke EM, Masaryk TJ, Wielopolski PA, et al. Optimizing blood vessel contrast three-dimensional MRI. Magn Reson Med 1989; 14:202–221.
20. Masaryk TJ, Modic MT, Ross JS, et al. Intracranial circulation: preliminary clinical results with three-dimensional (volume) MR angiography. Radiology 1989; 171:793–799.
21. Parker DL, Yuan C, Simons MA, Gulberg GT. Time of flight vessel imaging using multiple thin slab 3D acquisition. In: Book of abstracts: Society of Magnetic Resonance in Medicine, 1989; 1132.
22. Parker DL, Yuan C, Blatter DD. MR angiography by multiple thin slab 3D acquisition. Magn Reson Med 1991; 17:434–451.
23. Schmalbrock P, Chun Y, Chakeres DW, Kohli J, Pelc N. Volume MR angiography: methods to achieve very short echo times. Radiology 1990; 175:861–865.
24. Hoyt WF, Newton TH, Margolis MT. The posterior cerebral artery: section I—embryology and developmental anomalies. In: Newton TH, Potts DG, eds. Radiology of the skull and brain. Vol 2, Angiography. New York: Mosby, 1974; 1540–1550.
25. Haacke EM, Tkach JA, Parrish TB. Reduction of T2* dephasing in gradient field-echo imaging. Radiology 1989; 170:457–462.
26. Anderson CM, Saloner D, Tsuruda JS, Shapeero LG, Lee RE. Pictorial essay: artifacts in maximum-intensity-projection display of MR angiograms. AJR 1990; 154:623–630.
27. Ross JS, Masaryk TJ, Modic MT, Ruggieri PM, Haacke EM, Selman WR. Intracranial aneurysm: evaluation by intracranial MR angiography. AJNR 1990; 11:449–445.
28. Marchal G, Bosmans H, Van Fraeyenhoven L, et al. Intracranial vascular lesions: optimization and evaluation of three-dimensional time-of-flight MR angiography. Radiology 1990; 175:443–448.